Article f500057a

Cold-Start Durability of Membrane-Electrode Assemblies

C.Y. Wang, X.G. Yang[*], Y. Tabuchi[**], and F. Kagami[**]
Electrochemical Engine Center (ECEC), and Departments of Mechanical Engineering and Materials Science and Engineering, The Pennsylvania State University, University Park, PA 16802 USA

[*] Present address: Ford Motor Co.
[**] Nissan Motor Co. Ltd., Nissan Research Center, Kanagawa 237-8523, Japan

Abstract

Durability of membrane-electrode assemblies (MEAs) cycled under cold-start conditions is reviewed. It is shown that MEAs cycled under 100 mA/cm^2 from -30^{o}C show no degradation after 100 cycles, but exhibit mild degradation after 150 cycles under 300 mA/cm^2 from -30^{o}C, and furthermore suffer severe degradation after 110 cycles under 500 mA/cm^2 from -20^{o}C. Transmission electron microscopy (TEM) and X-ray diffraction using cross-sectional samples of the aged MEAs further revealed three primary degradation mechanisms: (i) interfacial delamination between the cathode catalyst layer (CL) and membrane, (ii) cathode CL pore collapse and densification upon melting of a fully ice-filled CL, and (iii) Pt particle coarsening and Pt dissolution in PFSA ionomer. The interfacial delamination and CL densification appear to be closely related to each other, and the key parameter to affect both is the ice volume fraction in the cathode CL after each cold-start step. Eliminating or minimizing these two degradation processes could improve the MEA cold-start durability by 280%. Mitigation strategies include improved gas purge prior to cold start, good MEA design, small startup current density, and low cell thermal mass.

1. Introduction

Cold-start capability and survivability of polymer electrolyte fuel cells (PEFCs) in a subzero environment is a major challenge for automotive applications. Recently, a series of experimental and theoretical studies have clarified the physics governing cold-start performance and led to the development of intraelectrode ice formation (IIF) theory.[1-11] The IIF theory shown in Fig.1 states that during cold start ice precipitates in the catalyst layer (CL) in two forms: as ice sheets between Pt particles and ionomer and as ice/frost grown into open pores. The ice sheets between Pt particles and ionomer lead to a Pt-area loss, which has been detected by subzero cyclic voltammetry[10]. The ice/frost appearing in open pores of the CL, confirmed by ex-situ cryo-SEM,[8,11] plugs the catalyst layer and starves reagent gases for oxygen reduction reaction. Areas that are plugged may then impose more stringent operating conditions on unplugged sections of the membrane-electrode assembly (MEA); i.e. current density in a partially blocked cell is redistributed to the remaining operable active areas. The increased local current density (and water production) exacerbates kinetic and transport deficiencies in remaining operating areas and further polarizes the cell in a cascading failure that may lead to cell voltage reversal and possible cell damage.

The cold-start problem is complex and comprehensive. As shown in Fig.2, the physics governing PEFC cold start are characterized by several disparate length scales. These range from the microscopic scale of the ionomeric structure in the proton-conducting membrane and triple-phase boundary in the CL, to the component level (membrane and CL), to the cell level. All of these are associated with different physical phenomena. At the microscopic scale, important physics include the state of water in perfluorosulfonic acid (PFSA) ionomer, proton and water transport mechanisms through the membrane, and ice/frost nucleation and growth from the triple-phase surface with mixed wettability. Of paramount importance at the component level are water adsorption or desorption rate in the membrane at very low temperatures, ice/frost filling of the catalyst layer, O_2 transport limitation, pore expansion and collapse upon phase transition, and the interfacial delamination between the membrane and catalyst layer during thermal cycling. At the cell level, the heat flow and current/water distributions play major roles in cold-start characteristics. Moreover, these multiscale phenomena are intimately coupled; for example, the ice/frost nucleation and growth at the microscopic scale strongly affects O_2 transport through the CL and hence the operational time of cold start at the cell level. On the other hand, the transport phenomena occurring at the cell level, prior to and during cold start, determine the temperature and water distributions, which in turn control ice/frost nucleation and growth at the microscopic scale of the cathode catalyst layer, and ice filling or melting in the CL at the component level.

The coupled nature of micro- and macro-scale phenomena in PEFC cold start explains why the cold-start discharge behavior is controlled not only by operating conditions such as the purge procedure, startup current density and temperature, but also by the materials properties such as membrane and CL design.

Figure 2 also illustrates various physical phenomena occurring at important stages of PEFC cold start. Four stages are defined along with the power and temperature profiles: shutdown (i.e. gas purge), cool down, cold start, and post-cold start. All the four stages have profound influences on fuel cell dynamics and durability undergoing cold-start cycles and hence should be fully understood. After shutdown, a purge process will remove liquid water from the gas channels, preventing ice formation and blockage there. In addition, the purge process will evaporate some liquid water from the GDL, CL and membrane in order to create room to store product water generated during cold start. During cool down, residual water vapor inside the fuel cell will condense inside micropores of the CL, occupying a fraction of the open pores in the CL. The liquid water trapped inside the CL micropores will turn into ice once the cell temperature drops below the freezing point. Ample evidence has demonstrated the profound importance of gas purge to PEFC cold start, and most recently the problem of gas purge has received rigorous fundamental treatment, both experimentally and analytically.[12,13]

The cool-down process is followed by cold start in which the fuel cell is discharged in galvanostatic or potentiostatic mode. The load produces both waste heat (desired) and product water (undesired). The amount of heat generation, after overcoming the cell thermal capacity, must raise the cell temperature above the freezing point before the catalyst layer is completely filled with ice and hence shut down. This is termed as successful self-startup. Clearly, the self-startup possibility hinges upon the delicate competition between heat generation (and resulting temperature rise) and water

production or ice formation. Also, the cell thermal mass and heat flow through the GDL between the catalyst layer and lands play a pivotal role in self-start. If water production completely fills the CL and shuts down the electrochemical reaction before the cell temperature exceeds the freezing point, the cell voltage experiences a drop down and the cold start fails unless there is external assist heating. Based on numerous experimental and theoretical results, the IIF theory has been found to adequately explain all physics involved in cold start and a computer model based on IIF theory has been devised to quantitatively predict the non-isothermal cold-start process under a myriad of operating conditions and MEA designs. See Refs.[9,14].

Once the fuel cell is successfully started, the ice inside the micropores melts. Intraelectrode ice melting (IIM) and subsequently liquid water removal from the CL at temperatures near the freezing point have not been touched upon in the open literature. In addition, the trapped liquid water may be evaporated and the pores may become accessible for gas transport before the CL is restored to full operation. There is a dire need to fully scrutinize the problem of post-cold start.

While significant advances have been made in understanding the principles of cold start, [1-14] little has been reported of MEA durability under cold-start cycling, and degradation mechanisms resulting specifically from cold start remain virtually unknown. In contrast, durability of PEFCs under dynamic conditions characteristic of automotive application has received much attention.[15,16] Membrane degradation, platinum dissolution and migration in PFSA ionomer, and carbon corrosion have been all extensively studied under various operating conditions including high cell potential, high temperatures, high or low humidity, as well as humidity/potential cycling and start/stop operation.[17-25]

2. Freeze/Thaw Cycling vs. Cold-Start Cycling

There are two types of cycling involved in the subzero storage and startup of automotive fuel cells. The first, freeze/thaw (F/T) thermal cycling, does not involve net water production in the cathode CL, and the other, cold-start cycling, does involve electrochemical production of water, thereby imposing a harsher condition for MEA durability. McDonald et al.[26] observed that the proton conductivity of Nafion 112 membrane does not change and no degradation in catalyst performance occurs for a dry MEA subjected to F/T cycling between –40 and 80^{o}C. Wilson et al.[27] showed that freezing at –10^{o}C is not detrimental to the MEA integrity despite its high water content. Cho et al. [28] reported that the performance of a cell containing membrane with high water content is degraded after F/T cycling between -10 and 80^{o}C. However, if the cell is purged with dry gas, almost no performance degradation or increase in membrane resistance can be observed after the F/T cycling.[29] Guo and Qi[30] showed that F/T cycles caused the catalyst layer (CL) of a fully hydrated MEA to crack, but did not lead to apparent damage to the CL if the cell was purged. While there has been much controversy in the literature on MEA durability from F/T cycles and its dependence on the membrane water content, the current consensus is that MEA can survive many hundreds of F/T cycles between a subzero temperature as low as -40^{o}C and an operating temperature as high as 80^{o}C. Therefore, MEA durability from F/T cycling has met the automotive requirement of subzero storage.

3. MEA Degradation under Cold-Start Cycling

Little has been published on MEA degradation resulting from cold-start cycling (with water production). Mao et al.[1] were among the first, and more recently Yang et al.[31] published a detailed report on MEA durability resulting from cold-start cycling. In the following, this latest work is reviewed in detail.

MEAs and cold-start cycling protocol - MEAs based on 30 μm fluorinated composite membrane were used, with Pt loading of 0.4mg/cm^2 at both anode and cathode. The corresponding catalyst layer was about 10 μm in thickness. Carbon paper with microporous layer was used as gas diffusion layers (GDL) on both anode and cathode sides. The cycling test protocol is schematically shown in Fig. 3.

Changes in polarization behavior during durability testing – A summary of three MEAs resulting from cold-start cycling is shown in Table 1, and their changes in polarization curve are depicted in Fig. 4. It can be seen that MEA #1, cycled from -30^{o}C at 100 mA/cm^2 startup current density, experienced virtually no degradation after 100 cycles. When the startup current density increased to 300 mA/cm^2, MEA #2, also cycled from -30^{o}C, suffered a mild degradation of only 13 mV at 1 A/cm^2 after 150 cycles. In contrast, when the current density increased to 500 mA/cm^2 (rapid cold start), MEA #3 cycled from -20^{o}C showed 330 mV degradation at 1 A/cm^2 after 110 cycles. In addition, Fig.4 shows that the HFR of MEA #3 increased appreciably between 95 and 110 cycles. Clearly, the startup current density is a significant factor influencing MEA durability resulting from cold start; as such, it is an important parameter to devise accelerated durability tests.

Breakdown of voltage losses – A breakdown of degradations in the kinetic, ohmic and mass-transport overpotential is shown in Fig. 5. For MEAs #1 and #2, a small increase in kinetic loss was observed, and overall the cell performance was minimally degraded. For MEA #3 (500mA/cm^2, -20^{o}C, 110 cycles), it is seen from Fig.5 that there is 120 mV increase in ohmic loss at 1 A/cm^2, 77 mV increase in kinetic loss, and 135 mV increase in mass-transport loss. Obviously, MEA degradation comes mainly from ohmic and mass-transport components. Furthermore, it is seen from Fig.4 that severe degradation started after 95 cycles. Detailed discussion on degradation mechanisms is deferred to a later subsection.

Microstructural and chemical changes – microstructural and chemical changes in aged MEAs were examined extensively by transmission electron microscopy (TEM), scanning electron microscopy (SEM), and X-ray diffraction (XRD) using cross-sectioned MEA samples.[31] Figure 6(a) shows a montage of the cathode CL in aged MEA #2 (300 mA/cm^2, -30^{o}C, 150 cycles) which experienced only mild degradation. It appears that the aged cathode exhibits relatively flawless microstructure, however, the interfacial layer within 0.5 μm close to the membrane displays some sign of densification (marked by dark color) and Pt particle coarsening (see Fig.6b). This may imply that severe degradation is imminent in this MEA after 150 cycles. The anode of this aged MEA #2 is shown in Fig.7. There is no obvious change in the anode microstructure. Indeed, high-magnification TEM images shown in Figs. 8 and 9 have captured several long strings of PFSA ionomer in the anode, also indicating that the aged anode remains relatively intact.

Figure 10 contrasts the TEM images of the interfacial regions of the aged cathode to the anode in MEA #2. It is evident that the anode/membrane interface remains a

porous structure, while that between the cathode/membrane shows signs of densification. This image, along with a more complete analysis of this aged MEA, indicates that there has not been severe degradation in this MEA; however, the degradation is imminent if given more cycles and will first occur in the cathode CL.

The microstructural and chemical changes occurring in MEA #3 (500 mA/cm^2, -20^{o}C, 110 cycles) were examined in great detail.[31] As mentioned earlier, there was a total of 330 mV degradation in cell performance at 1 A/cm^2. Moreover, this cold-start cycle (500 mA/cm^2, -20^{o}C) is interesting as it represents a possible accelerated test protocol for studies of MEA degradation resulting from cold start. SEM cross-section images of the entire MEA #3 suggested that the anode thickness remained at ~10μm while that of the cathode shrank to only 4.3 μm over 110 cycles. As will be explained shortly, the cathode CL shrinkage results from the pore collapse and hence CL densification, thereby exacerbating the mass-transport loss.

Another distinctive observation of MEA #3 is the interfacial delamination between the cathode CL and membrane, as clearly detected by the low-magnification TEM image shown in Fig.11. The localized delamination is responsible for the increase in ohmic loss of the aged MEA by ~120 mV. The interfacial delamination and CL densification appear closely related to each other. Figure 12 shows a montage of TEM images for the aged cathode where the cathode CL is seen to be around 5 μm, confirming the SEM finding. In addition, a gap between the cathode CL and membrane is clearly visible from Fig.12.

Aside from the interfacial delamination and CL thinning/densification, MEA #3 also experiences Pt area loss as confirmed by cyclic voltammograms shown in Fig.13. It is seen that the Pt area determined by CV is significantly reduced over cycles. The other interesting information observable from these voltammograms is that the double-layer charging current does not change with cold-start cycle, indicating that the area of carbon in contact with ionomer is unchanged. This experimental evidence clearly supports that there is negligible carbon corrosion in cold-start cycling despite the presence of start/stop and that the cathode CL thinning does not result from carbon corrosion but from cold start, or more specifically from ice formation during cold start.

Figure 14 compares TEM image of the fresh cathode with that of the aged cathode in MEA #3. It is found that the size of Pt particles increases from the initial 3 nm to 5-8 nm; this particle growth alone decreases the specific surface area by 50% in the aged cathode. Pt ripening and dissolution in the aged cathode was also confirmed by X-ray diffraction.[31] Two mechanisms of Pt area loss in normal operation of a PEFC are well known: Pt particle ripening and Pt dissolution in PFSA ionomer. The kinetics of both are expected to depend strongly on temperature. It is thus surprising to find profound Pt particle growth and dissolution in the ionomer under cold-start conditions. One possible explanation is that strong voltage cycling involved in cold-start cycles predominantly controls the Pt particle growth and dissolution. The Pt area loss in this aged MEA is responsible for ~77 mV kinetic loss after 110 cycles. When Pt is dissolved in PFSA ionomer and diffused into the membrane where Pt cations are subsequently reduced by crossover hydrogen from the anode, large Pt crystals form inside the membrane. This process clearly takes place in aged MEA #3 as shown in Fig.15. Based on the above Pt precipitation mechanism, the location of Pt precipitation depends on the diffusivity of Pt ions and H_2 crossover rate. Under cold-start conditions, H_2 crossover is retarded, which

may cause Pt precipitation to occur on the anode side of the membrane, as detected by the TEM image shown in Fig.15. In contrast, under normal operation the Pt band is commonly seen close to the cathode side of the membrane.[18,32,33] Further research should be conducted on Pt dissolution and Pt band formation in the membrane under cold-start conditions.

4. Degradation Mechanisms and Mitigation Strategies

According to the IIF theory, parameters strongly influencing the amount of ice formed in the cathode include the initial membrane water content (effected by gas purge), startup current density, startup temperature, MEA design, and cell thermal mass. The theory predicts that the higher the startup current density, the more ice formed in the cathode CL. Also, under high current densities, ice distributes more towards the CL/GDL interface.

Degradation mechanisms from cold start – Based on the IIF theory and the above-described durability test data and microstructural/chemical analysis, we hypothesize three primary mechanisms of MEA degradation occurring in cold start: (1) interfacial delamination between the membrane and cathode CL, (2) Pt particle growth and Pt dissolution in PFSA ionomer, and (3) cathode CL structural damage and hence densification. The interfacial delamination is believed to be responsible for the 120 mV increase in ohmic loss in MEA #3 as observed in Fig.5(c), and Pt area loss due to coarsening and dissolution could contribute to the 77 mV increase in kinetic loss. Note that Pt coarsening and dissolution take place under normal cell operation and are not a unique problem of cold start. Therefore, any advances in mitigating Pt area loss under normal operation would benefit MEA durability from cold start as well.

The third degradation mechanism involving CL structural damage and likely densification is responsible for the 135 mV increase in mass-transport loss in MEA #3. CL densification is a plausible explanation for the increased mass-transport loss and is also consistent with the hypothesis of interfacial delamination because CL densification will most likely leave additional space or partial vacuum in the CL/membrane interfacial region which could peel the CL off the membrane. We hypothesize that the cathode CL thinning and densification results from melting of a completely ice-filled CL. This ice melting results in volume shrinkage, vacuum creation and finally pore collapse. In the high current density cycling for MEA #3, most of the product water accumulates in the cathode CL, thereby completely filling it. That is, the volume fraction of ice may have reached nearly 100% of the pore volume. The high ice fraction residing in the cathode CL is then subject to melting once the cell temperature breaks through the freezing point. Melting causes the volume shrinkage and hence creation of localized vacuum. Local vacuum will exert pressure and stress upon the CL structure. Once the stress created from vacuum exceeds the integrity pressure of the CL network, the pore structure in CL will partially collapse, thereby resulting in a denser CL. The shrunken CL will also detach from the membrane, causing interfacial delamination. Per this hypothesis, we believe that the CL densification and interfacial delamination are closely related, and solving one problem will avoid the other at the same time.

The mechanism of CL pore collapse and densification also explains why an MEA can sustain many hundreds of freeze/thaw cycles between -40^{o}C and 80^{o}C. During freeze/thaw thermal cycling, there is no net water production and the water or ice level

residing in the CL never changes nor reaches close to 100% so long as adequate gas purge is carried out prior to thermal cycling. Therefore, during freezing or melting, there is sufficient open space in the CL porous structure to absorb volume changes without causing CL structural damage.

Mitigation strategies – The key to improving MEA durability from cold start is clearly to mitigate interfacial delamination and CL densification. For MEA #3, this will remove 77mV ohmic loss and 135 mV mass-transport loss out of a total 330 mV degradation, meaning a 280% improvement in durability. According to the afore-presented analysis, a key parameter is the ice fraction in the cathode CL before melting, and a high level is to be avoided for improved MEA durability. This suggests that freeze/thaw thermal cycles should incorporate the practice of gas purge. Cold-start cycles should avoid the voltage drop-down period as much as possible. The CV study of Ge and Wang[7] clearly showed that it is in this voltage drop-down period that ice accumulates substantially in the cathode CL (possibly reaching a level close to 100% of all void spaces according to ex-situ cryo-SEM results of Thompson et al.[8] and Li et al.[11]). Known techniques to minimize the ice fraction in the cathode CL and hence achieve better MEA durability include good purge practice to maintain relatively dry membranes prior to cold start, small startup current density, high startup temperature, low cell thermal mass, good MEA design, and current ramping with temperature[14].

5. Summary and Outlook

Literature research on MEA durability resulting from cold start has found three principal degradation mechanisms: (i) interfacial delamination between the cathode CL and membrane, (ii) cathode CL pore collapse and densification, and (iii) Pt area loss due to particle ripening and dissolution in PFSA ionomer. The interfacial delamination and CL densification are closely tied to each other, and the key parameter to affect both appears to be the ice volume fraction in the cathode CL after each cold start process. If the ice fraction reaches close to 100% of the pore volume in CL, volume extraction upon subsequent ice melting will occur, thereby resulting in localized vacuum and hence CL pore collapse, CL densification and interfacial delamination.

It is thus implied that the ability to measure and control the ice fraction inside the cathode CL holds the key to understanding and mitigating the dramatic MEA degradation under harsh cold-start conditions. The subzero CV technique to detect the presence of ice between Pt and ionomer in the CL is a first step in this direction,[10] and more innovative research should be encouraged to develop *in-situ* techniques to measure and monitor the ice amount in the cathode CL.

Acknowledgements

We acknowledge Nissan Motor Co. Ltd., Penn State Materials Research Institute, and NSF under grant no. 0609727 for the writing of this chapter. Contributions made by former and current members of the ECEC cold-start team over the last seven years are gratefully acknowledged.

References

1. L. Mao, K. Tajiri, S. Ge, X. G. Yang, and C. Y. Wang, Abstract 998, The Electrochemical Society Meeting Abstracts, Vol. 2005-2, Los Angeles, CA, Oct. 16-21, 2005.
2. S. Ge and C.Y. Wang, *Electrochem. & Solid-State Lett.*, **9**, A499 (2006).
3. L. Mao and C.Y. Wang, *J. Electrochem. Soc.*, **154**, B139 (2007).
4. K. Tajiri, Y. Tabuchi, and C.Y. Wang, *J. Electrochem. Soc.*, **154**, B147 (2007).
5. L. Mao, C.Y. Wang, and Y. Tabuchi, *J. Electrochem. Soc.*, **154**, B341 (2007).
6. K. Tajiri, Y. Tabuchi, F. Kagami, S. Takahashi, K. Yoshizawa, and C.Y. Wang, *J Power Sources*, **165**, 179 (2007).
7. S. Ge and C.Y. Wang, *Electrochim. Acta*, **52**, 4825 (2007).
8. E.L. Thompson, J. Jorne, and H.A. Gasteiger, *J. Electrochem. Soc.*, **154**, B783 (2007).
9. F.M. Jiang, W.F. Fang and C.Y. Wang, *Electrochim. Acta*, **53**, 610 (2007).
10. S. Ge and C.Y. Wang, *J Electrochem Soc*., **154**, B1399 (2007)
11. J. Li, S. Lee, and J. Roberts, *Electrochim. Acta*, in press (2008).
12. P.K. Sinha and C.Y. Wang, *J Electrochem Soc.*, 154, B1158 (2007).
13. K. Tajiri, C.Y. Wang and Y. Tabuchi, *Electrochim. Acta*, in press (2008).
14. F.M. Jiang and C.Y. Wang, *J Electrochem Soc.*, in press (2008).
15. S.D. Knights, K.M. Colbow, J. St-Pierre, and D.P. Wilkinson, *J. Power Sources*, **127**, 127 (2004).
16. M.F. Mathias, R. Makharia, H.A. Gasteiger, J.J. Conley, T.J. Fuller, C.J. Gittleman, S.S. Kocha, D.P. Miller, C.K. Mittelsteadt, T. Xie, S.G. Yan, and P.T. Yu, *Electrochem. Soc. Interface*, **14**, 24 (2005)
17. J. Xie, D.L. Wood III, K.L. More, P. Atanassov, and R.L. Borup, *J Electrochem Soc.*, **152**, A1011 (2005).
18. P.J. Ferreira, G.J. la O, Y. Shao-Horn, D. Morgan, R. Makharia, S. Kocha, and H.A. Gasteiger, *J Electrochem. Soc*., **152**, A2256 (2005).
19. X. Wang, R. Kumar, and D. J. Myers, *Electrochem. Solid-State Lett.*, **9**, A225 (2006).
20. T. Yoda, H. Uchida and M. Watanabe, *Electrochim. Acta*, **52**, 5997 (2007).
21. E. Endoh, S. Terazono, H. Widjaja, and Y. Takimoto, *Electrochem. Solid-State Lett.*, **7**, A209 (2004).
22. V. O. Mittal, H. R. Kunz, and J. M. Fenton, *Electrochem. Solid-State Lett.*, **9**, A299 (2006).
23. A. Ohma, S. Suga, S. Yamamoto, and K. Shinohara, *J Electrochem Soc*., **154**, B757 (2007)
24. B. Sompalli, B.A. Litteer, W.B. Gu, H.A. Gasteiger, *J Electrochem. Soc.*, **154**, B1349 (2007).
25. C.A. Reiser, L. Bregoli, T.W. Patterson, J.S. Yi, J.D. Yang, M.L. Perry, and T.D. Jarvi, *Electrochem. Solid-State Lett*, **8**, A273 (2005)
26. R.C. McDonald, C. K. Mittelsteadt, and E. L. Thompson, *Fuel Cells*, **4**, 208 (2004).
27. M. S. Wilson, J. A. Valerio, and S. Gottesfeld, *Electrochim. Acta*, **40**, 355 (1995).
28. E. A. Cho, J. J. Ko, H. Y. Ha, S. A. Hong, K. Y. Lee, T. W. Lim, and I. H. Oh, *J. Electrochem. Soc.*, **150**, A1667 (2003).

29. E. A. Cho, J. J. Ko, H. Y. Ha, S. A. Hong, K. Y. Lee, T. W. Lim, and I. H. Oh, *J. Electrochem. Soc.*, **151**, A661 (2004).
30. Q. Guo and Z. Qi, *J. Power Sources*, **160**, 1269 (2006).
31. X.G. Yang, Y. Tabuchi, F. Kagami and C.Y. Wang, *J. Electrochem. Soc.*, in press (2008).
32. J. Zhang, B.A. Litteer, W.B. Gu, H. Liu, and H.A. Gasteiger, *J. Electrochem. Soc.*, **154**, B1006 (2007).
33. W. Bi, G.E. Gray, and T.F. Fuller, *Electrochem. & Solid-State Lett.*, **10**, B101 (2007).

Table 1 Summary of cold-start cycle test results [31]

	MEA #1	MEA #2	MEA #3
Current Density	100 mA/cm^2	300 mA/cm^2	500 mA/cm^2
Temperature	-30^{o}C	-30^{o}C	-20^{o}C
Cycle Number	100 cycles	150 cycles	110 cycles
Degradation Range @ 1 A/cm^2 & 70^{o}C	No degradation	0.561 to 0.548 V	0.588 to 0.257 V
Delamination	no	no	severe
CL Densification	no	mild	severe
Pt Coarsening	no	mild	severe

List of Figures

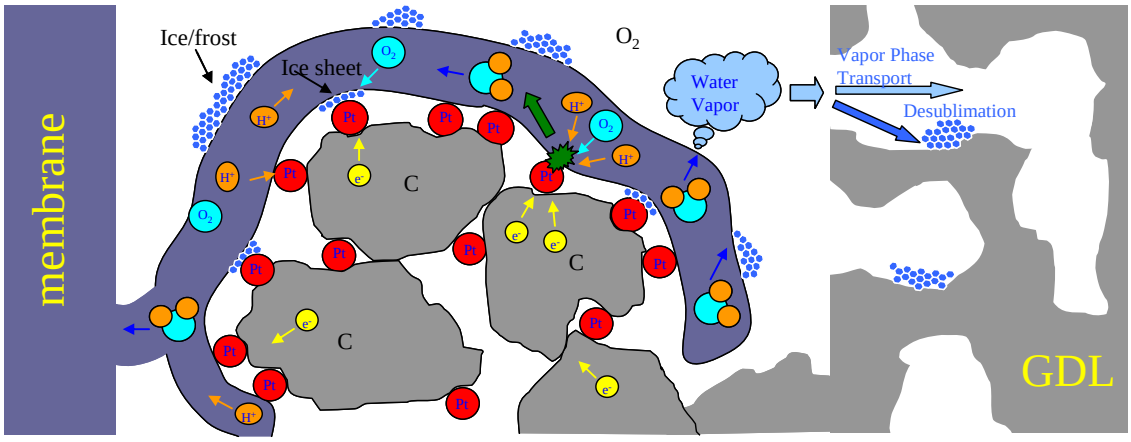

Figure 1. Schematic illustration of intraelectrode ice formation (IIF) theory, showing micro-scale ice distribution in the cathode catalyst layer.

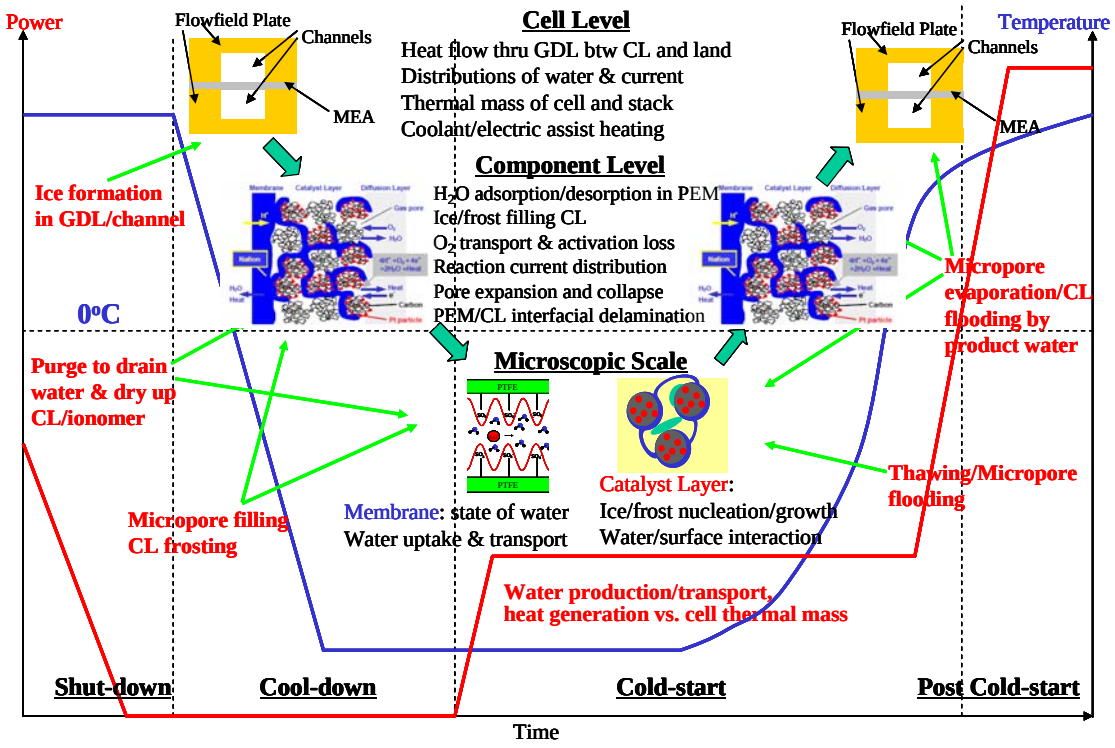

Figure 2. Schematic illustration of the multi-scale physics of PEFC cold start

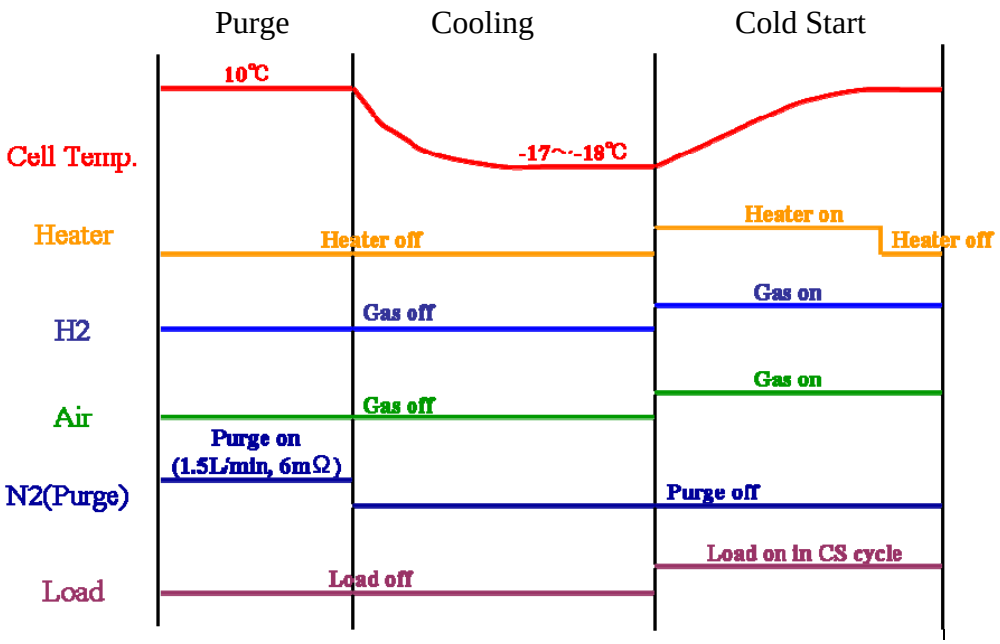

Figure 3. Cold-start cycling procedure

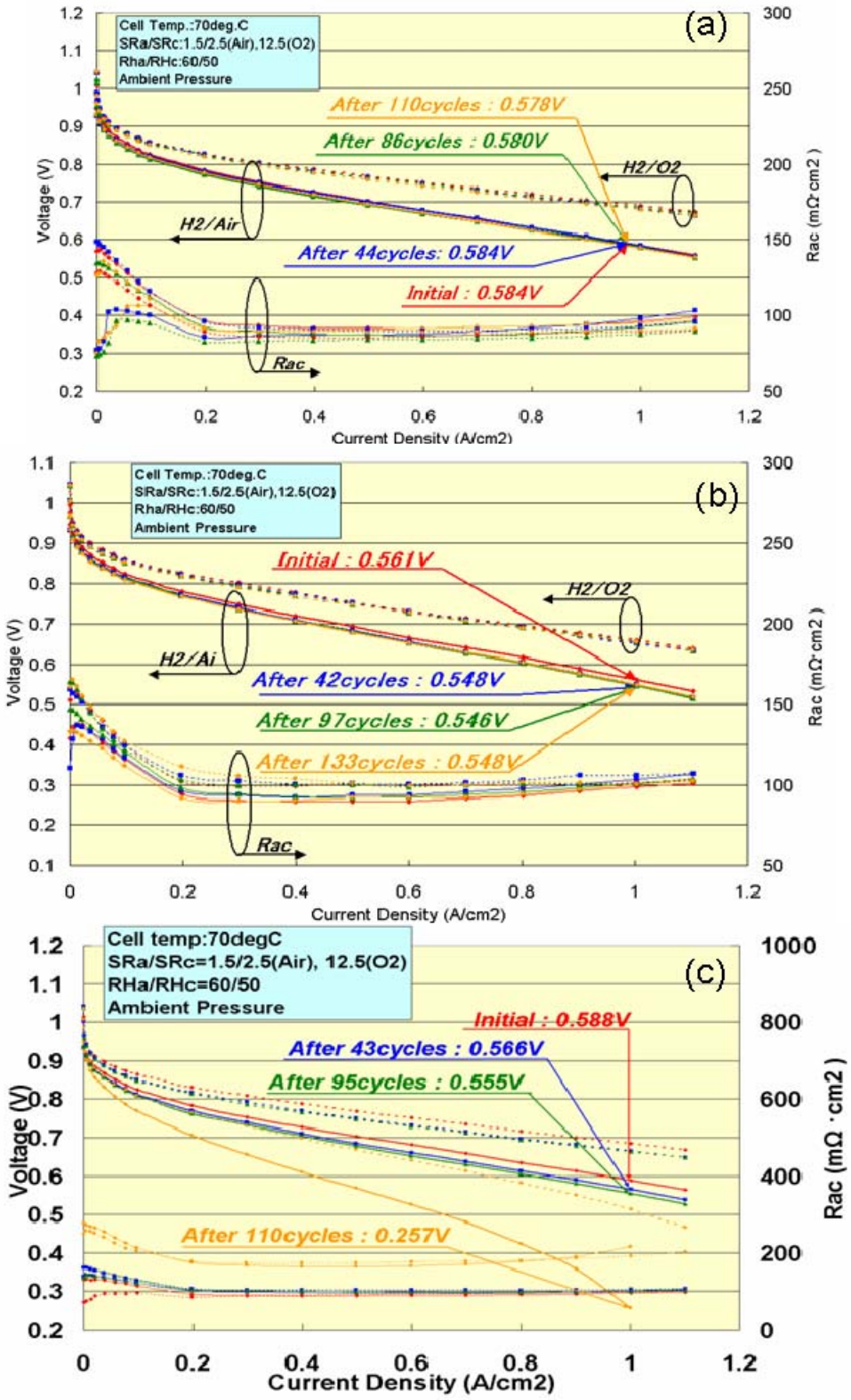

Figure 4 Polarization curves after cold-start cycles for: (a) MEA#1, (b) MEA#2, and (c) MEA#3 as listed in Table 1

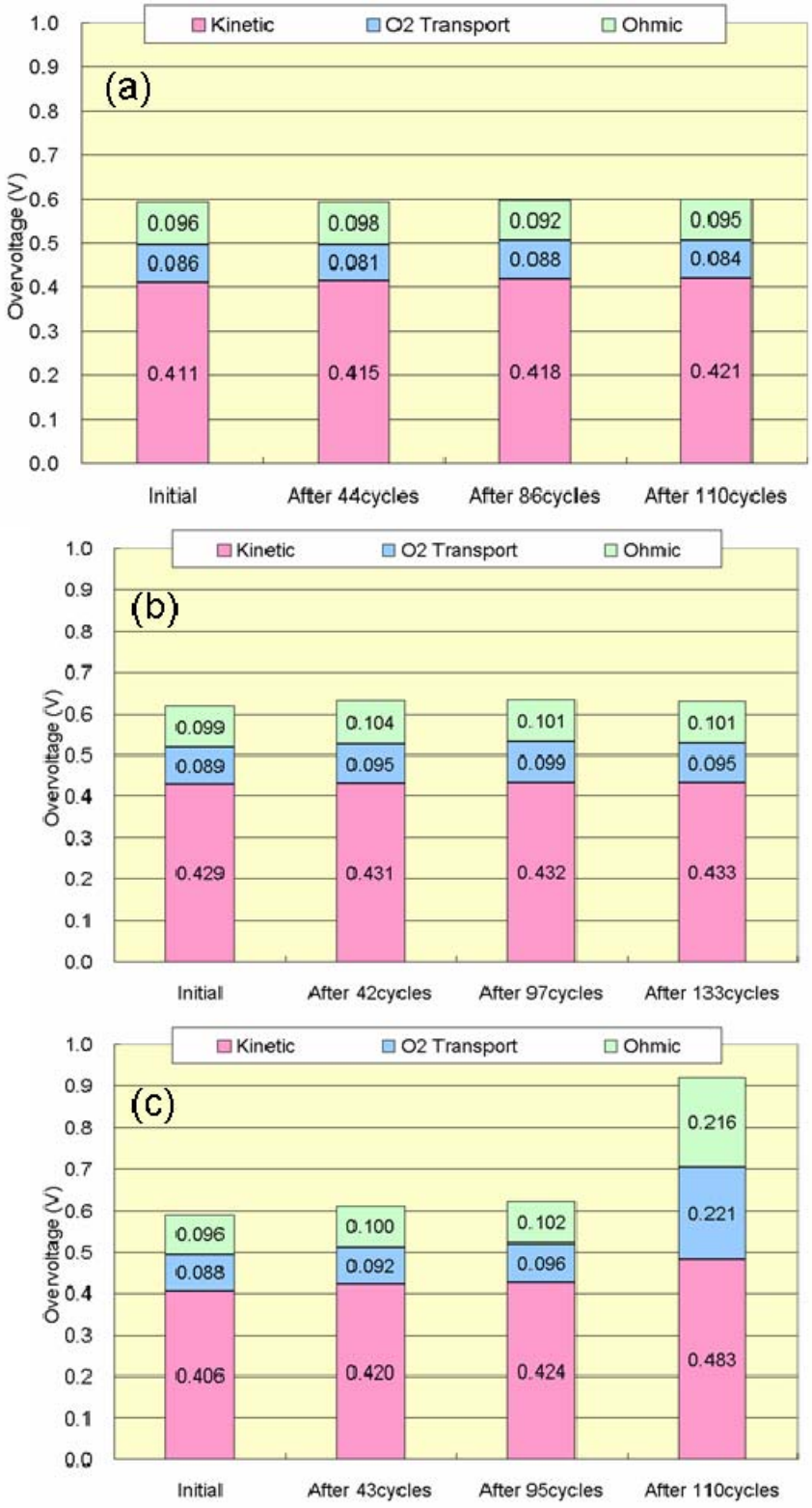

Figure 5 Results of overpotential breakdown at 1 A/cm^2 and 70^{o}C for: (a) MEA#1, (b) MEA#2, and (c) MEA#3.

(a)

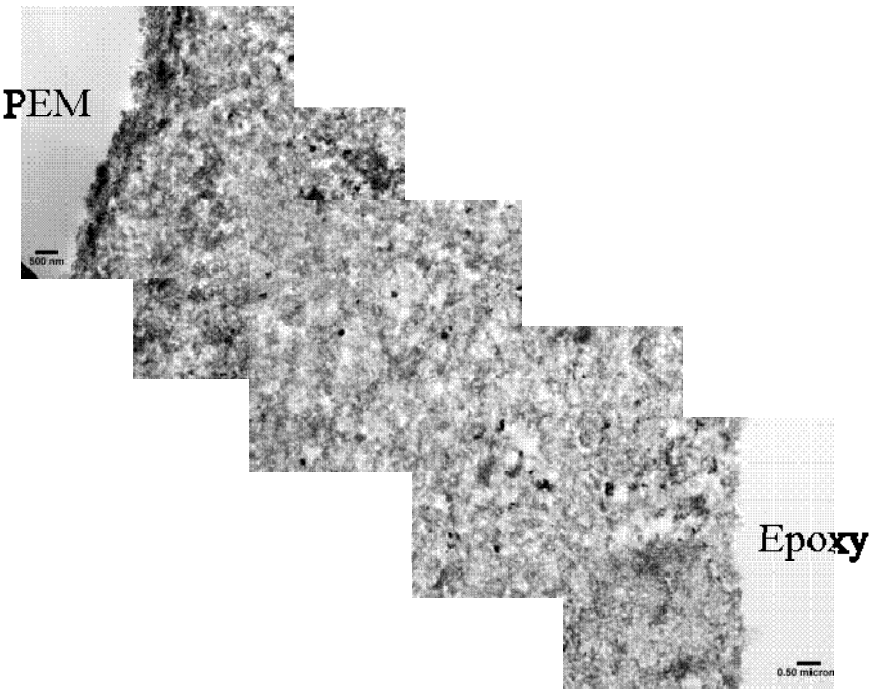

(b)

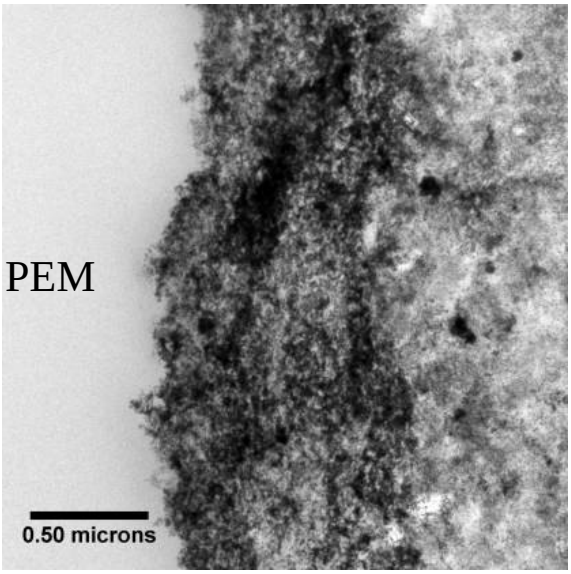

Figure 6. TEM images of aged MEA #2 (300 mA/cm^2, -30^{o}C, 150 cycles), showing: (a) the whole cathode catalyst layer, and (b) the interface between the membrane and cathode catalyst layer.

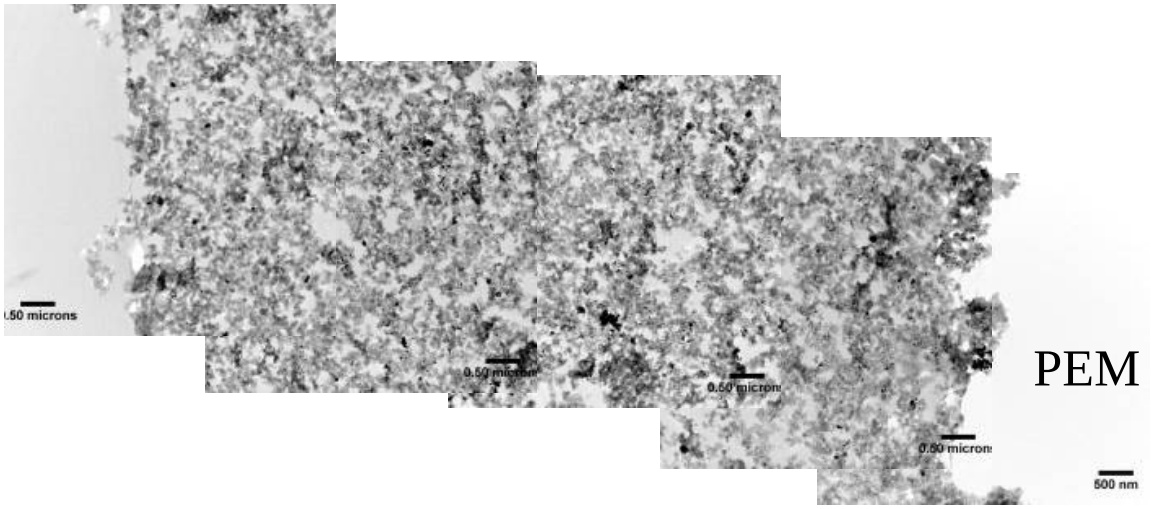

Figure 7. Microstructure of the aged anode in MEA #2 (300 mA/cm^2, -30^{o}C, 150 cycles).

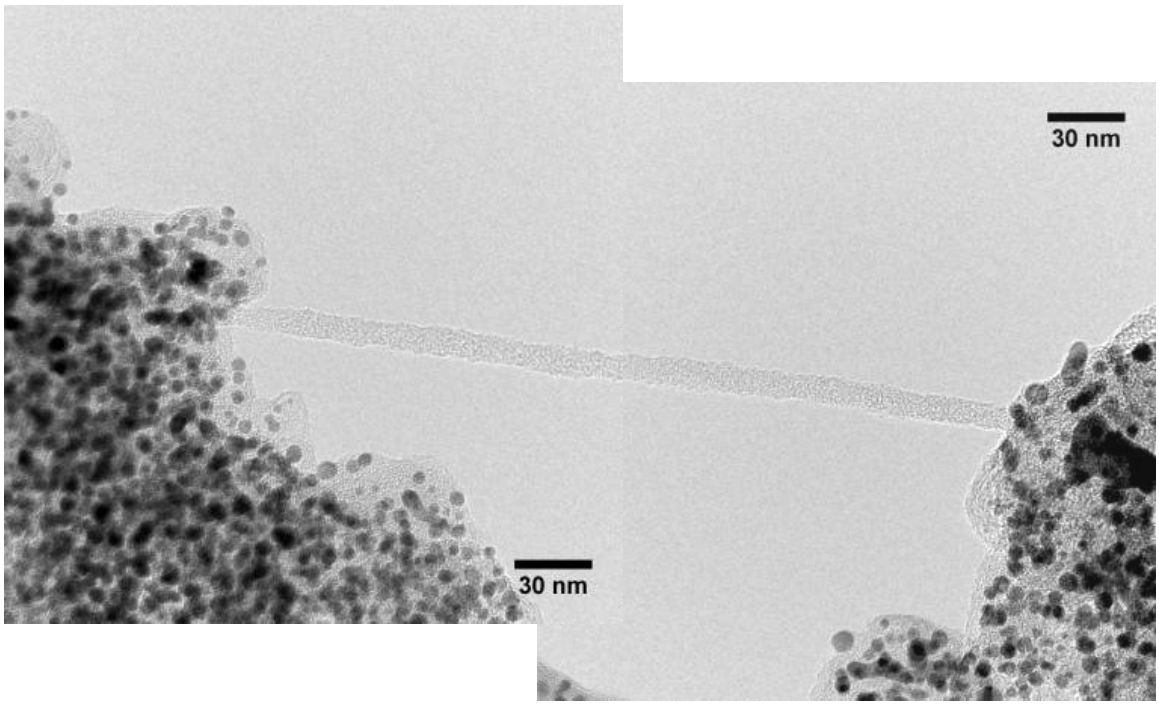

Figure 8. A long string of ionomer in the aged anode of MEA #2 close to the membrane, indicating preservation of the anode microstructure.

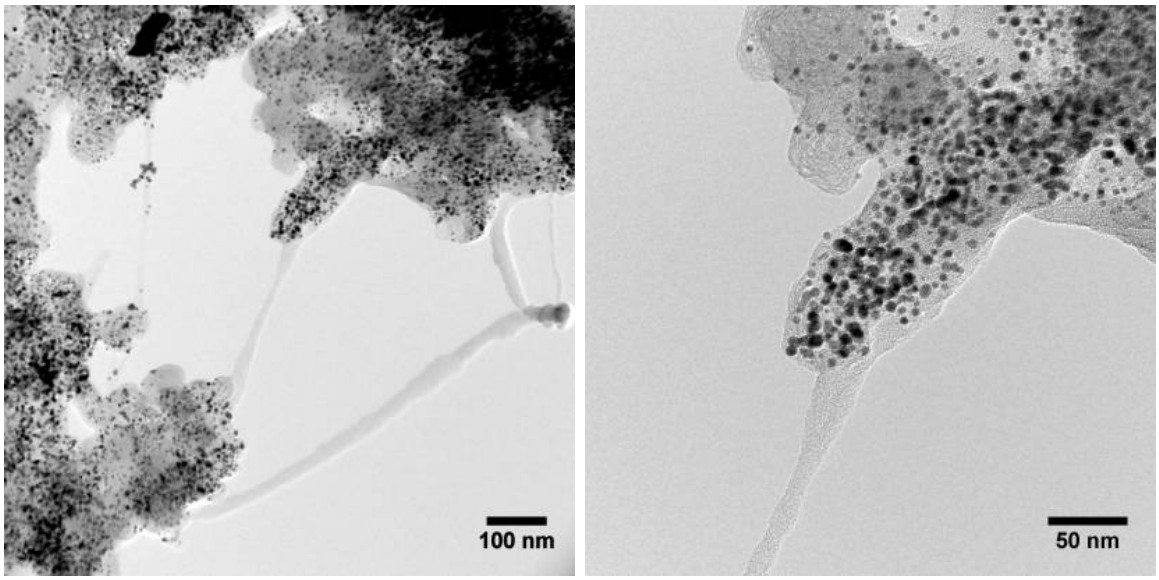

Figure 9. TEM images of ionomer network in the aged anode of MEA #2 (300 mA/cm^2, -30^{o}C, 150 cycles).

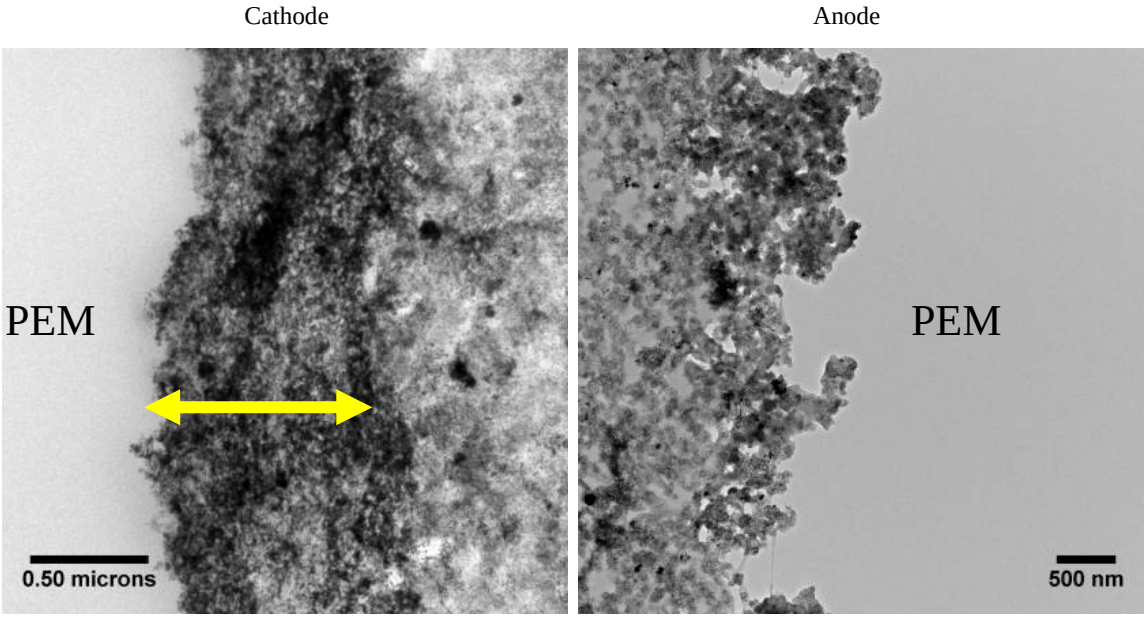

Figure 10. Comparison of the PEM/CL interfacial regions between aged cathode and anode of MEA #2.

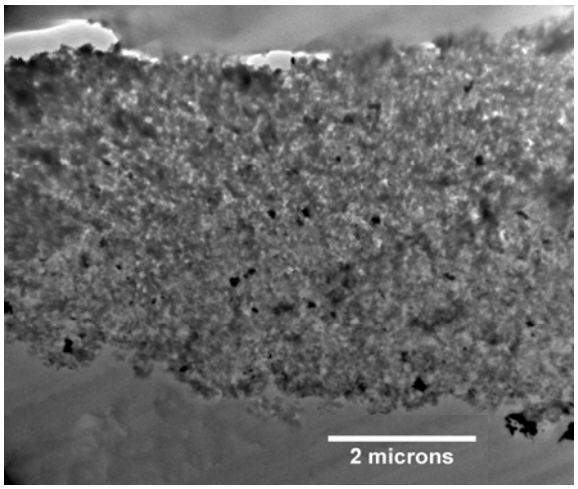

Figure 11. Low-magnification TEM image of the cathode CL in MEA #3 showing localized delamination between the CL and membrane.

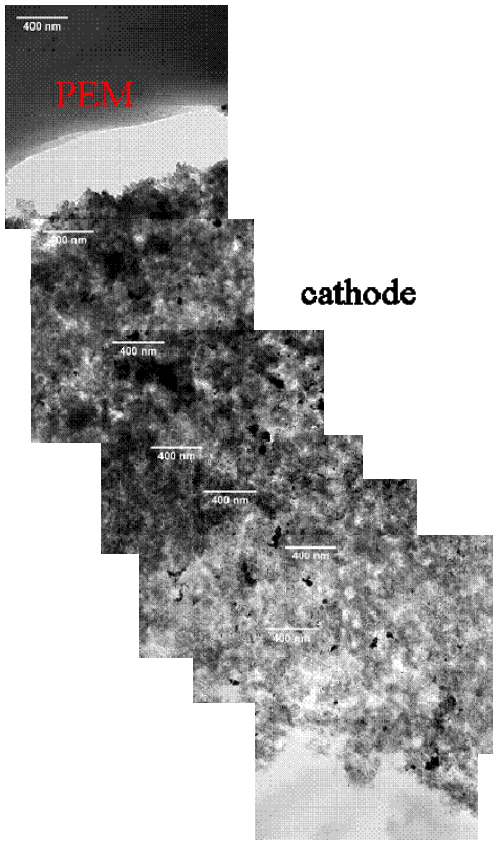

Figure 12. TEM images of the cathode catalyst layer in aged MEA #3 (500mA/cm^2, -20^{o}C, 110 cycles)

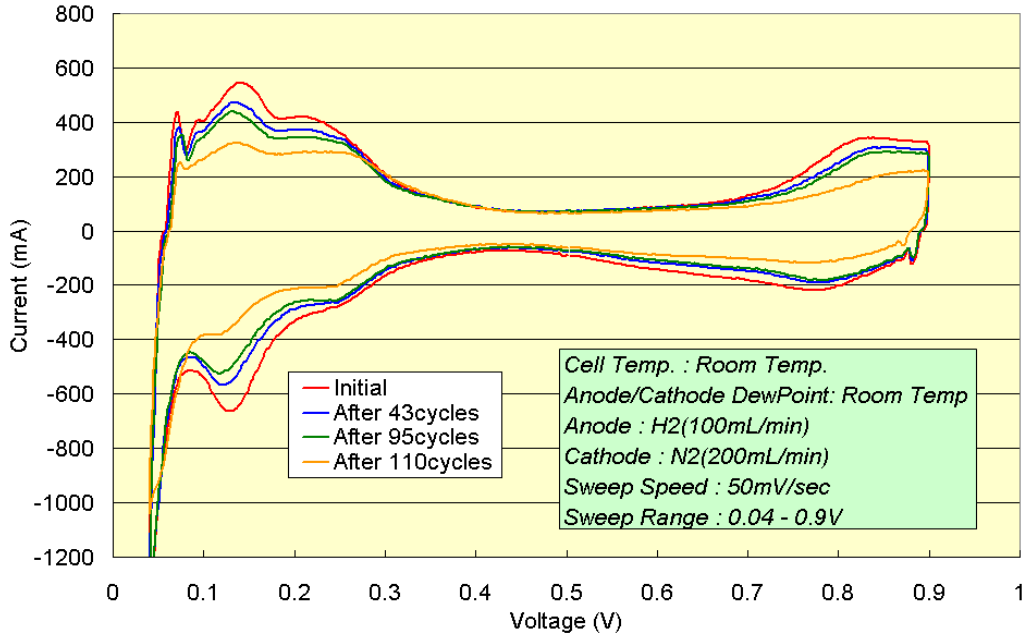

Figure 13. Cyclic voltammograms for MEA #3 (500mA/cm^2, -20^{o}C, 110 cycles) at various stages of ageing.

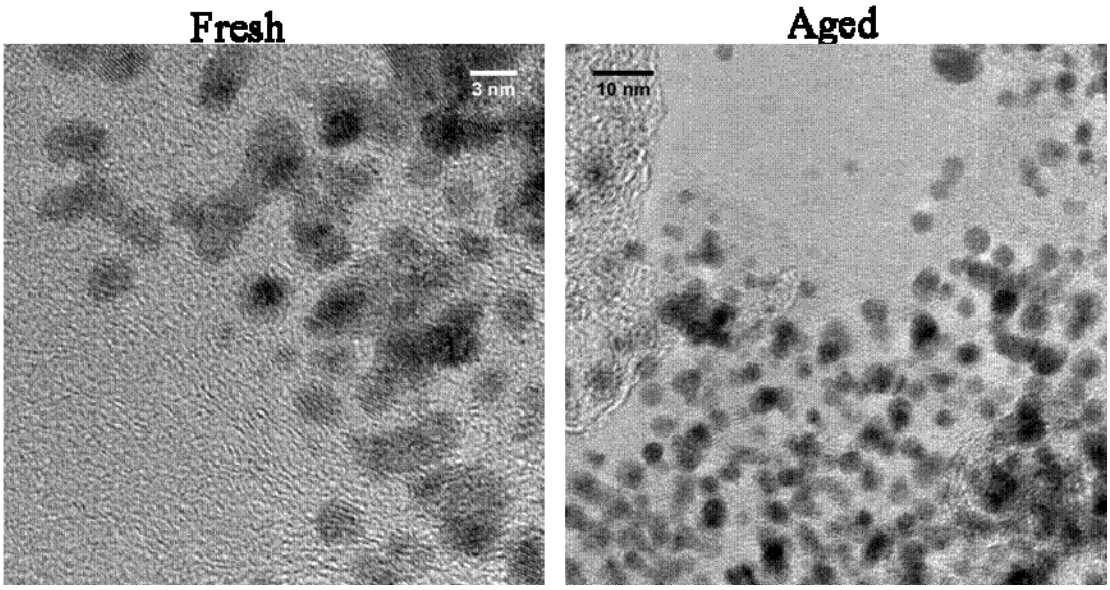

Figure 14. Comparison of HR-TEM images of the cathode catalyst layer between fresh MEA and aged MEA #3 (500mA/cm^2, -20^{o}C, 110 cycles)

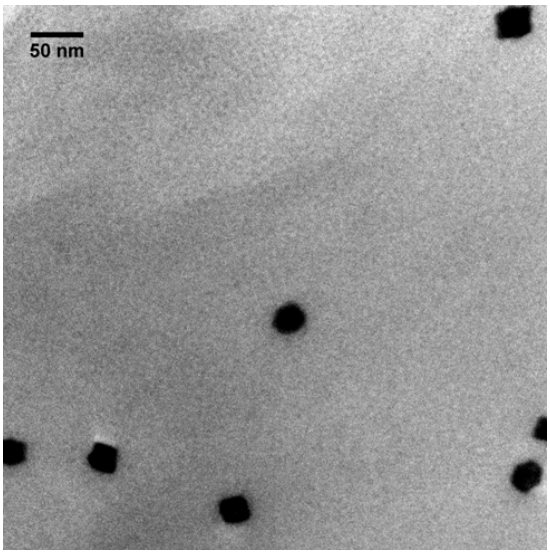

Figure 15. TEM image of large, square-shaped Pt crystals on the anode side of the membrane in MEA #3, confirmed by EDX.